Experimental example of isotropic surface second-harmonic generation: dc-sputtered air-exposed aluminum thin films

Charles W. Teplin* and Charles T. Rogers
Department of Physics, University of Colorado at Boulder, Boulder, Colorado 80309-0390
(Received 26 November 2001; published 29 May 2002)

We have determined the amplitudes and relative phases of the allowed components of the effective surface second-harmonic susceptibility, $\chi^{(2)}$, for a set of air-exposed dc-sputtered Al thin films. The second-harmonic intensity and polarization state was measured as a function of linear input polarization state and azimuthal orientation of the sample using a Ti:sapphire laser at 810 nm. The films are found to be optically isotropic with respect to azimuthal rotation angle, consistent with an isotropic $\chi^{(2)}$ with seven elements in three families. Using measured linear optical properties, the elements of $\chi^{(2)}$ were determined from the data. In terms of the dimensionless parameters a, b, and d [J. Rudnick and E. A. Stern, Phys. Rev. B **4**, 4274 (1971)], we find $|a|=2.30\pm0.72$, in rough agreement with previous measurements of the surface current perpendicular to the surface on oxidized Al surface, $|b|=0.013\pm0.004$ for the surface current parallel to the surface, and $|d|=0.009\pm0.002$ for the bulk contribution. The relative phases of a and b with respect to d are found to be $(-0.4\pm6)°$ and $(63\pm12)°$, respectively. The measurement indicates a large discrepancy between measured values and the universal theoretical expectation that $b=-1$ and $d=1$.

DOI: 10.1103/PhysRevB.65.245408 PACS number(s): 78.20.−e, 42.65.Ky

I. INTRODUCTION

Optical second-harmonic generation (SHG) is a powerful tool for studying the properties of surfaces and interfaces in condensed matter systems, particularly those with cubic or isotropic bulk structure.[1] In systems of this type, SHG is dominated by dipolar response near the symmetry-breaking surfaces and interfaces and bulk magnetic dipole and electric quadrupole response; it therefore provides a direct probe of surface and interface properties for any interface accessible optically. A great deal of theoretical and experimental effort has focused on developing an understanding of SHG in various situations.

Microscopic theories for SHG from the surface of cubic metals have existed for more than 30 years.[2] Initial efforts concentrated on Boltzmann equation and electron gas hydrodynamics calculations of the nonlinear surface current $\vec{J}_S^{(2)}$ due to surface dipolar response, and calculations of the nonlinear bulk current $\vec{J}_B^{(2)}$ due to bulk magnetic dipole and electric quadrupole response, proportional to $\vec{E}\times\vec{B}$. These early theories succeeded in setting the scale and identifying major sources of surface response. They also helped demonstrate the sensitivity of results for the surface current perpendicular to the surface, $J_{S,Z}^{(2)}$, to the detailed surface structure. Since the work of Rudnick and Stern,[3] effort has focused on calculations of the dimensionless parameters $a(\omega)$ and $b(\omega)$ that, respectively, characterize the nonlinear surface currents perpendicular and parallel to the surface, and $d(\omega)$ that characterizes the nonlinear bulk current [see Eq. (7) below]. For example, Leibsch and Schaich[4] (LS) have used a self-consistent jellium model for the sample surface, and find $a=-32-4i$ at $\lambda=0810$ μm and electron densities similar to the observed Al density. All theoretical treatments of isotropic metal surfaces with which we are familiar agree that $b(\omega)=-1$ and $d(\omega)=1$ but find various results for $a(\omega)$ depending on details of the calculated or assumed electronic density profile near the surface. All of this work is in good qualitative agreement with Rudnick and Stern's original argument, namely, that while hydrodynamics is adequate for calculations of the bulk nonlinear current and the surface currents parallel to the surface, $J_{S,Z}^{(2)}$ is sensitive to surface structure.

Aluminum is an easily prepared, nearly free-electron metal, which has been used extensively for fundamental surface SHG studies. In particular, the observed values of $a(\omega)$ for ultrahigh vacuum (UHV) prepared Al(111) surfaces have been found to be described semiquantitatively by theoretical treatments using the jellium approximation, probably indicating a very smooth ionic potential for this surface.[5,6] These experiments have also demonstrated that SHG from UHV-prepared Al(111) and Al(100) is often not isotropic with rotation about surface normal, thereby motivating further work on anisotropic SHG.[7]

In an initial attempt to confirm the predictions of LS, Murphy *et al.*[5] report good agreement with the result of $|a|=37$ for UHV Al(111) surfaces at $\lambda=1.064$ μm. On Al(100) and polycrystalline Al surfaces, their measurements found $|a|=22$. Measurements by Janz *et al.*[6] on UHV Al(111) and Al(110) single crystals also show qualitative agreement with the results for values of $a(\omega)$ from LS over a wide wavelength range. Their results for $a(\omega)$ on Al(100) surfaces show good agreement with the experimental results of Murphy *et al.* Additionally, measurements in their laboratory found that *p*-polarized SHG for *p*-polarization incident light decreased by a factor of roughly 10 when UHV Al surfaces were oxidized.[8] Experiments on air-exposed polycrystalline Al and Al(100) surfaces by Pedersen and Keller[9] found that $|a|$ was similar in magnitude to b and d, but are not well fitted by an isotropic model. Lastly, measurements of Al/glass interfaces[10] showed that a was near to unity. Collectively, these results show a reasonable degree of agreement between theory and experiment for the overall magni-

tude of the surface sensitive parameter $a(\omega)$ for UHV (111) surfaces. Additionally, experimental results show that Al(100) surfaces and Al surfaces that have intermediate oxide or glass layers exhibit effectively smaller values for a.

Previous experimental work, however, has been less clear in its measurements of $b(\omega)$ and $d(\omega)$. This has been, in part, because previous SHG experiments on UHV Al surfaces have focused on measurements of the *p*-input, *p*-output geometry, which exhibits the largest second-harmonic yield. This geometry is largely sensitive to $a(\omega)$, though $b(\omega)$ and $d(\omega)$ also contribute. In comparison, $b(\omega)$ controls the yield of *s*-polarized SHG due to a mixed *s*- and *p*-polarized input beam, while $d(\omega)$ controls the *p*-polarized SHG from pure *s* input. These geometries are typically observed to have much lower SHG yields. Thus, few detailed comments on measured values of b and d from Al surfaces are presently available. Murphy *et al.* found strong anisotropy in SHG and made few comments on b or d. Janz *et al.* did not detect any *s*-polarized second-harmonic light for any wavelength or incident polarization. Nor did they detect any second-harmonic light for *s*-polarized incident light. These results indicate that their measured values for $b(\omega)$ and $d(\omega)$ were indistinguishable from zero, a surprising result considering the general expectation that these parameters are of order unity and are robust to detailed surface conditions. Additionally, we note the surprising findings of Simpson and Furtak,[11] who found that $d(\omega)$ was sensitive to the charging of the surface of single-crystal Ag in an electrochemical environment. Again, this measurement indicates a discrepancy with the theoretical models that expect the bulk contribution to be insensitive to the details of the surface. Finally, previous measurements of SHG from free-electron-like metals provide little or no information on the relative phases of a,b, and d.

In this work, we report a measurement of the elements (both their magnitude and relative phases) of the effective surface second-harmonic susceptibility tensor $\chi^{(2)}$ for air-exposed polycrystalline, Al thin films. These films were chosen because they are easily prepared, technologically important, and expected to yield straightforward, isotropic behavior that would allow for simple analysis. Our measurements of the intensity and polarization state of surface second-harmonic light as a function of input beam polarization and azimuthal angle of the Al sample are well described by an isotropic model for surface SHG. The success of this model allows for the determination of the absolute values and relative phases of a, b, and, d. This analysis clearly indicates that b and d are much smaller than theoretical predictions and indicates the need for a deeper understanding of these parameters.

The rest of this paper is organized as follows. In Sec. II, we provide an overview of the theoretical model for SHG from an isotropic surface. Section III explains the details of the experimental apparatus we used to measure the second-harmonic intensity and polarization state as a function of sample azimuthal angle and input beam polarization state. This section also includes analysis of the second-harmonic data and shows that our results are consistent within statistical error of the model in Sec. II. In Sec. IV, we explain measurements of sample surface morphology and linear optical constants and use these measurements to deduce the numerical values of the susceptibility tensor elements. In Sec. V our experimental results for the magnitudes and relative phases of the tensor elements are compared to previous measurements and theoretical models. Finally, conclusions from this work are discussed in Sec. VI.

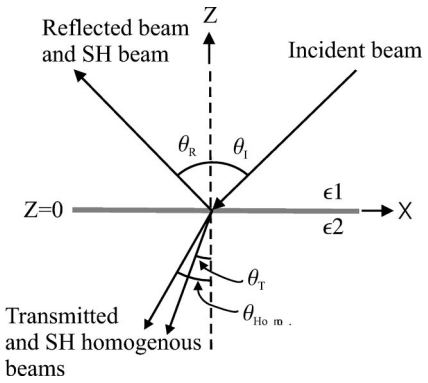

FIG. 1. Coordinate system showing the optical beams. The incident beam is transmitted at an angle, θ_T, and reflected at an angle θ_R. Second-harmonic inhomogeneous (driven) and homogeneous beams propagate into at angles θ_T and $\theta_{Homo.}$. Second-harmonic light is reflected at angle θ_R.

II. THEORETICAL MODEL FOR SECOND-HARMONIC GENERATION FROM AN ISOTROPIC SURFACE

For a surface scientist, the goal of a surface SHG experiment is to measure surface properties via their influence on the second-harmonic currents at the surface of a material. Quite generally, the Cartesian components of these currents may be written as

$$\frac{J_{S,i}^{(2)}}{-2\imath\omega}=P_{S,i}^{(2)}=\chi_{S,ijk}^{(2)}E_j e^{-\omega t}E_k e^{-\omega t}. \tag{1}$$

Here, $J_S^{(2)}$ is the surface current density at twice the fundamental frequency ω, $P_S^{(2)}$ is the dipole moment per unit area in the dipole approximation, $\chi_{S,ijk}^{(2)}$ is the second-harmonic surface susceptibility tensor, and E_i is the ith component of the electric field at the fundamental frequency at the surface of the material. These currents are manifest by the reflected optical intensity at 2ω.

As shown by Shen,[1] the nonlinear boundary conditions at the surface imply that a nonlinear surface polarization radiates in the following way:

$$E_P^{(2)}=\frac{\imath 4\pi k_1}{\epsilon_2 k_{1z}+\epsilon_1 k_{2z}}(k_{2z}P_{S,x}^{(2)}+k_x P_{S,z}^{(2)}),$$

$$E_S^{(2)}=\frac{\imath 4\pi k_1}{k_{1z}+k_{2z}}\frac{k_1}{\epsilon_1}P_{S,y}^{(2)}. \tag{2}$$

Here, k_i is the wave vector at 2ω in medium i, $k_{i,z}$ is the z component of the wave vector at 2ω, and $\epsilon_{i,2\omega}$ is the dielectric constant at 2ω in medium i. As shown in Fig. 1, the surface normal is taken to be in the $\hat{z}$ direction and the opti-

cal plane of incidence is the $\hat{x}$-$\hat{z}$ plane. The surface polarization at 2ω arises from the electric fields present at the surface of the material through the susceptibility tensor as in Eq. (1). As has been shown previously,[1] the susceptibility tensor can be simplified extensively for an isotropic surface. In the coordinate system of Fig. 1, the nonzero tensor elements for an isotropic surface occur in three distinct families: $\chi^{(2)}_{ZZZ}, \chi^{(2)}_{ZXX}=\chi^{(2)}_{ZYY}$, and $\chi^{(2)}_{XZX}=\chi^{(2)}_{XXZ}=\chi^{(2)}_{YZY}=\chi^{(2)}_{YYZ}$. With these tensor elements, the surface polarizations can be written as

$$
\begin{aligned}
P^{(2)}_{S,x} &= (\chi^{(2)}_{XXZ}+\chi^{(2)}_{XZX}) t_P^2 \sin\theta_T \cos\theta_T \cos^2\phi E_I^2 ,\\
P^{(2)}_{S,y} &= (\chi^{(2)}_{YYZ}+\chi^{(2)}_{YZY}) t_P t_S \sin\theta_T \sin\phi\cos\phi E_I^2 ,\\
P^{(2)}_{S,z} &= (\chi^{(2)}_{ZZZ}\sin^2\theta_T+\chi^{(2)}_{ZXX}\cos^2\theta_T) t_P^2 \cos^2\phi E_I^2 \\
&\quad + \chi^{(2)}_{ZYY} t_S^2 \sin^2\phi E_I^2 ,
\end{aligned}
\tag{3}
$$

where t_P is the Fresnel transmission coefficient for *p*-polarized light, t_S is the Fresnel transmission coefficient for *s-polarized light*, θ_T *is the transmitted complex angle*, ϕ *is the angle of the incident polarization from p* polarization (so *p* occurs at 0° and 180° and *s* occurs at 90° and 270°), and E_I is the incident electric field magnitude.

In addition to radiation at 2ω from induced surface currents, second-harmonic radiation also arises from nonlinear currents in the bulk of the metal. As has been shown previously,[3] these currents arise from a quadrupolar effect proportional to $\vec{E}\times\vec{B}$ in the bulk of the material. Thus, the nonlinear bulk currents are in the direction of the transmitted wave vector. These currents radiate *p*-polarized electric fields:[1]

$$
E^{(2)}_P = \frac{\imath 4\pi k_1}{\epsilon_2 k_{1z}+\epsilon_1 k_{2z}} k_x \gamma (t_S^2 \sin^2\phi + t_P^2 \cos^2\phi) E_I^2 , \tag{4}
$$

where γ characterizes the bulk nonlinear susceptibility.

From Eqs. (2)–(4), we can write the radiated *p*- and *s*-polarized second-harmonic fields as

$$
\frac{E^{(2)}_P}{E_I^2} = \frac{\imath 4\pi k_1}{\epsilon_2 k_{1z}+\epsilon_1 k_{2z}} \left\{ \begin{array}{l} t_P^2 \cos^2\phi \left[+ k_x \left(\begin{array}{c} k_{2z}\sin\theta_T\cos\theta_T(\chi^{(2)}_{XZX}+\chi^{(2)}_{XXZ}) \\ \sin^2\theta_T(\chi^{(2)}_{ZZZ}+\gamma) \\ +\cos^2\theta_T(\chi^{(2)}_{ZXX}+\gamma) \end{array} \right) \right] \\ + t_S^2 \sin^2\phi k_x (\chi^{(2)}_{ZYY}+\gamma) \end{array} \right\} \tag{5}
$$

and

$$
\frac{E^{(2)}_S}{E_I^2} = \frac{\imath 4\pi k_1}{k_{1z}+k_{2z}} \frac{k_1}{\epsilon_1} t_S t_P \sin\phi\cos\phi\sin\theta_T (\chi^{(2)}_{YZY}+\chi^{(2)}_{YYZ}). \tag{6}
$$

From these equations, it is clear that experimentally one cannot separate the bulk radiation from surface terms, particularly $\chi^{(2)}_{ZXX}$ and $\chi^{(2)}_{ZYY}$.[12] Quite generally, all the theoretical models of surface SHG from isotropic surfaces with which we are familiar predict that the surface tensor elements, $\chi^{(2)}_{ZXX}=\chi^{(2)}_{ZYY}$, are zero due to the continuity of the transverse component of the incident electric field. Because of this expectation, for the remainder of this work, we will neglect $\chi^{(2)}_{ZXX}$ and $\chi^{(2)}_{ZYY}$ (but see Sec. V below), replace γ with an effective susceptibility element, $\chi^{(2)}_{BULK}, \chi^{(2)}_{XZX}=\chi^{(2)}_{XXZ}=\chi^{(2)}_{YZY}=\chi^{(2)}_{YYZ}$ with $\chi^{(2)}_{\parallel}$, and $\chi^{(2)}_{ZZZ}$ with $\chi^{(2)}_{\perp}$. In the notation of Rudnick and Stern, these effective tensor elements can then be written as[3]

$$
\chi^{(2)}_{\perp} = a(\omega)\left(\frac{e}{16\pi m\omega^2}\right)[\epsilon(\omega)-1],
$$

$$
\chi^{(2)}_{\parallel} = b(\omega)\left(\frac{e}{16\pi m\omega^2}\right)[\epsilon(\omega)-1],
$$

$$
\chi^{(2)}_{BULK} = d(\omega)\left(\frac{e}{16\pi m\omega^2}\right)[\epsilon(\omega)-1], \tag{7}
$$

where e is the charge of the electron, m is the electron mass, and $\epsilon(\omega)$ is the dielectric function at angular frequency ω.

III. EXPERIMENTAL MEASUREMENTS OF ISOTROPIC SHG

The experimental apparatus (Fig. 2) is designed to measure the polarization state of the second-harmonic light produced by an 80 mW average power Ti:sapphire laser beam (100 MHz pulse rate, 50 fs pulse duration, 810 nm central wavelength) focused onto an Al film (roughly 10 μm spot diameter) at a 45° angle of incidence. The polarization of the input beam is varied by using a half wave plate to rotate the polarized output of the laser followed by a Glan-Taylor polarizer to ensure the purity of the polarization state. The angle of the wave plate and the polarizer are controlled remotely with stepper motors that allow for 25 steps between *s*

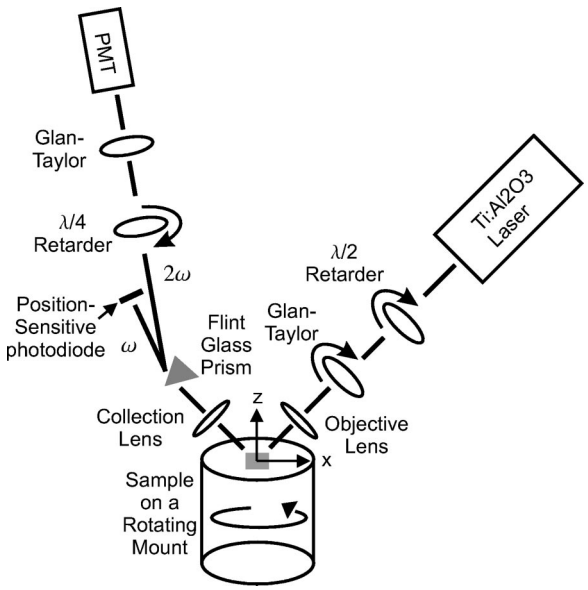

FIG. 2. Experimental apparatus.

and *p* polarization. An objective lens with a small effective numerical aperture of 0.06 is used to focus the beam onto the sample in order to preserve the input polarization state. A second lens collects the reflected laser beam and the second-harmonic light from the sample. A flint glass prism is used to spatially separate the much weaker second-harmonic light from the reflected primary beam in order to facilitate optical analysis. Anti-reflection coatings on the prism reduce the polarization sensitivity to below 1% of transmission difference between *s*- and *p*-polarized incident waves.

We used this apparatus to measure SHG from a variety of air-exposed Al films. The films were grown by dc sputtering with a simultaneous rf bias onto a growth substrate of 1000 Å SiO_2 (thermally grown oxide) on Si(100) from a 99.999% pure Al target.[13] For the different films, the rf bias, growth rate, and growth time were varied in order to acquire a range of different film properties. X-ray diffraction data from characteristic Al films produced in our growth chamber suggest that the films are (111) textured, with random orientation in the plane of the film. The surface roughness and thickness for seven different films for which we present data are listed in Table I.

We measured the intensity and polarization state of the second-harmonic light with a rotating-wave-plate polarimeter. The polarimeter consists of a remotely stepped zeroth order quarter wave plate followed by a linear polarizer oriented to pass *p* polarization and a photo-multiplier tube. The intensity of the polarimeter throughput is measured as a function of quarter-wave-plate angle. During each polarization measurement, the wave plate is spun many times and the average intensity and the average deviation from the average intensity is calculated. The resulting data and statistical error is fitted to a function of the Stokes parameters, $S1$,$S2$, and $S3$ that completely describe the intensity and polarization state of the light through

$$S1 = I_P - I_S,$$

$$S2 = I_{45} - I_{-45},$$

$$S3 = I_{RCP} - I_{LCP}. \tag{8}$$

Here, $I_P, I_S, I_{45}, I_{-45}, I_{RCP}$, and I_{LCP} are the intensities of *p*, *s*, 45°, −45°, right-circularly polarized, and left-circularly polarized light, respectively. $S0$, the Stokes parameter identifying the total intensity of the light, is found within experimental error to satisfy $S0^2 = S1^2 + S2^2 + S3^2$, indicating that the second harmonic has no unpolarized component. During fitting, therefore, we set $S0^2 = S1^2 + S2^2 + S3^2$ and fit for only $S1$,$S2$, and $S3$. Typical values of χ^2 per degree of freedom, the square of the average deviation of the fit from the data normalized to the square of the measured statistical deviation from the average measured value (not to be confused with $\chi^{(2)}$, the nonlinear susceptibility) for these fits were close to unity. Calibration of the offset from *p* polarization in the linear polarizer and the actual retardation and offset from *p* polarization in the wave plate is achieved using standard *p* polarized and nearly circularly polarized input light to the polarimeter.

We then study the polarization state of the second-harmonic beam as a function of polarization state of the incident Ti:sapphire beam. Due to imperfections in the half

TABLE I. Properties of Al film samples. Film thicknesses for samples 1–5 are estimated from growth conditions. Film thicknesses for samples 6 and 7 are determined from ellipsometric fits. The complex parameters η (with phase ϕ_η) and κ (with phase ϕ_κ) characterize the isotropic second-harmonic response for each film, as shown in Eqs. (9) and (10).

Sample	Roughness (Å) (rms)	Thickness (Å)	$\lvert\eta\rvert$	$\lvert\kappa\rvert$	ϕ_η (degrees)	ϕ_κ (degrees)
1	25	600	2.89±0.02	0.58±0.01	18.1±0.3	−80.4±0.5
2	29	400	2.69±0.02	0.50±0.01	25.2±0.6	−59.9±0.3
3	24	1070	3.12±0.02	0.57±0.01	25.1±0.7	−51.2±0.3
4	16	1070	3.03±0.03	0.57±0.01	25.0±0.9	−60.7±0.6
5	17	1070	3.17±0.02	0.51±0.01	25.2±0.6	−55.2±0.2
6	14	312	2.37±0.02	0.73±0.01	20.2±0.7	−43.7±0.3
7	12	332	2.93±0.04	0.83±0.01	26.4±0.6	−48.1±0.6

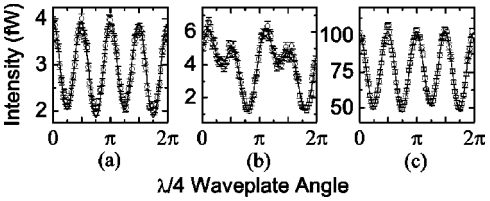

FIG. 3. Measured intensity as a function of polarimeter quarter-wave-plate angle for input polarization angle of (a)89, (b)67, and (c)1° for Sample 1. Solid lines show the fit to the polarization state of the second-harmonic beam. In case (a), the incident beam is nearly *s* polarized and the fitting results in $S1=4.06\pm0.02$ fW, $S2=-0.26\pm0.06$ fW, $S3=0.18\pm0.03$ fW, and $\chi^2=1.5$, showing that the second-harmonic beam is nearly *p* polarized, but of low intensity. In case (b), the incident beam is a linearly polarized, but with *p*- and *s*-polarized components and the fitting results in $S1=3.41\pm0.07$ fW, $S2=-4.28\pm0.10$ fW, and $S3=3.24\pm0.06$ fW and $\chi^2=1.0$, showing that the second-harmonic light has both *p*- and *s*-polarized components. In case (c), the input beam is nearly *p*-polarized and the fit results in $S1=107.02\pm0.24$ fW, $S2=-3.54\pm0.91$ fW, $S3=1.24\pm0.41$ fW, and $\chi^2=1.2$, showing that the second-harmonic beam is intense and close to *p* polarization.

wave plate and linear polarizer on the input arm of the apparatus, we found that the input intensity varied by approximately 5% as the incident polarization state is changed. To compensate for this variation, we took data for a complete rotation of the half-wave-plate (two rotations of the linear polarizer, four rotations of the polarization vector). Polarimetry data and the fitted Stokes parameters for three example input polarizations are shown in Fig. 3 for Sample 1 from Table I. We can then use the measured Stokes parameters to determine I_S, I_P, and their relative phase $\delta=\phi_S-\phi_P$. Figure 4 shows I_S, I_P, and δ for Sample 1 for all input polarizations averaged over the four rotations of the polarization vector. Significant uncertainty in δ, the relative phase of the *s*-polarized electric field to the *p*-polarized electric field, occurs near *s*- and *p*-input polarization because the *s*-output intensity is approaching zero.

The entire set of second-harmonic Stokes parameters versus incident light polarization was then measured at 32 discrete sample azimuthal angular positions (32 different rotational positions about the surface normal). Wobble in the sample rotation mount was measured by placing a position-sensitive quadrant photodiode[14] in the path of the intense, reflected beam. We then adjusted a two-axis tilt stage that held the sample to minimize the difference signals from the quadrant photodetector, thereby aligning the sample normal and the azimuthal axis of rotation. For all films measured, the data shows that the intensity and polarization state of the second-harmonic light is independent of sample azimuthal angle to $\pm5\%$. Figure 5 shows the variation in the second-

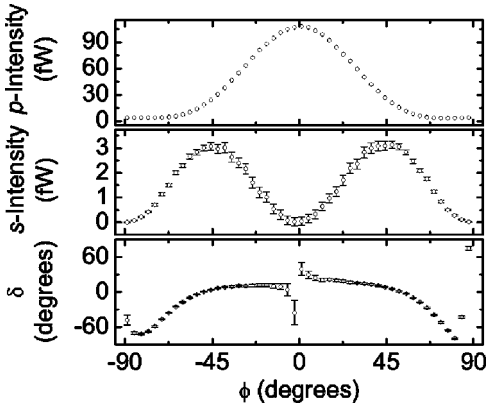

FIG. 4. Second-harmonic light *p*-polarization intensity, *s*-polarization intensity, and relative phase $\delta=\phi_S-\phi_P$ generated as a function of input polarization angle for Sample 1. This data has been averaged over a full rotation of the input polarization optics, or four complete rotations of the input polarization state. (Input *p*-polarization corresponds to 0°. Input *s* polarization corresponds to 90°.)

harmonic *s* intensity, *p* intensity, and relative phase δ of the *s* and *p* second-harmonic electric fields as a function of azimuthal angle for Sample 1. For this measurement, the input polarization angle was set to $\phi=70°$ so that the output polarization was sensitive to all nonzero tensor elements. In this configuration, the different polarization state parameters varied by $\pm5\%$ as the azimuthal angle was varied. We associate this residual variation with observed higher-order wobble in our mount that could not be eliminated with a simple, two-axis tilt stage.

The azimuthal data confirm that our Al films are isotropic second-harmonic sources. Therefore, the model summarized in Eqs. (5) and (6) is appropriate for analysis of the second-harmonic data as a function of input polarization state. The *s* to *p* intensity ratio and relative phase δ of the *s* and *p* electric fields were, therefore, fitted to the following functions:

$$\tan\Psi^{(2)}\equiv\frac{|E_S^{(2)}|^2}{|E_P^{(2)}|^2}=\frac{\sin^2\phi\cos^2\phi}{(\eta\cos^2\phi+\kappa\sin^2\phi)^2} \tag{9}$$

and

$$\delta=\arctan\left[\frac{\mathrm{Im}(\eta\cos^2\phi+\kappa\sin^2\phi)}{\mathrm{Re}(\eta\cos^2\phi+\kappa\sin^2\phi)}\right]. \tag{10}$$

Here, Im denotes ''the imaginary part of'' and Re denotes ''the real part of.'' The data was fitted to $\tan\Psi^{(2)}$ and δ simultaneously, resulting in values and associated uncertainty for the complex parameters η and κ, which are given from Eqs. (5), (6), (9), and (10) for the isotropic model by:

$$\eta=\frac{k_{1z}+k_{2z}}{\epsilon_2 k_{1z}+\epsilon_1 k_{2z}}\frac{\epsilon_1}{k_1}\frac{t_P}{t_S}\frac{2k_{2z}\cos\theta_T\sin\theta_T\chi_{\parallel}^{(2)}+k_x[\sin^2\theta_T(\chi_{\perp}^{(2)}+\chi_{BULK}^{(2)})+\cos^2\theta_T\chi_{BULK}^{(2)}]}{2\sin\theta_T\chi_{\parallel}^{(2)}} \tag{11}$$

and

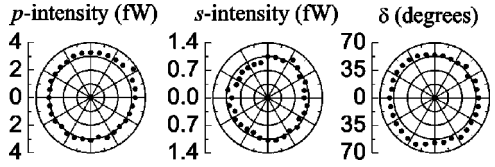

FIG. 5. Second-harmonic polarization variation as a function of sample azimuthal angle for an incident beam with polarization angle, ϕ, of 70° for sample 1. At this input polarization angle, the nonlinear response is sensitive to all nonlinear susceptibility tensor elements. The variation in the parameters is approximately $\pm 5\%$ and is attributed to residual wobble in the sample mount.

$$\kappa = \frac{k_{1z}+k_{2z}}{\epsilon_2 k_{1z}+\epsilon_1 k_{2z}} \frac{\epsilon_1}{k_1} \frac{t_S}{t_P} \frac{k_x \chi^{(2)}_{BULK}}{2\sin\theta_T \chi^{(2)}_{\parallel}}. \tag{12}$$

δ was not fitted near *s*- and *p*-incident polarization.[15] The fit for the data shown in Fig. 4 is shown in Fig. 6 for all four quadrants of equivalent input polarization angle and the fitted values of η and κ and their associated statistical error are shown in Table I. The χ^2 for the fit shown in Fig. 6 was 3.7 and the fits for all other films resulted in χ^2 values between 3 and 13. The success of these fits demonstrates that the isotropic model described above accurately accounts for our results. Polycrystalline Al films of this type are excellent ''textbook'' examples of isotropic SHG.

IV. ANALYSIS OF RESULTS TO EXTRACT $\chi^{(2)}$

Our direct observation of isotropic second-harmonic response (Fig. 5), along with the success of Eqs. (9) and (10) in fitting the experimental results leads us to consider a deeper analysis of the data sets, aimed at extracting the actual values of the second-harmonic tensor elements. While the measurements reported above are definitive in demonstrating that the SHG in these films is accurately isotropic and consistent with a minimal set of surface SHG elements as demanded by the symmetry considerations, it is nevertheless essential to recognize that further analysis is, by necessity, model dependent. Many isotropic models are possibly consistent with the observed intensity and polarization states. Just as in ellipsometry, the reflected far-field wave can be accurately calculated given a known surface, but the reflected wave does not itself contain enough information to allow inversion to determine surface properties. However, such a model-dependent inversion is necessary to allow direct comparison with existing theory. In this section, we discuss our efforts to develop an internally consistent model of the film morphology that explains both the linear and the nonlinear optical response. This model allows us to extract a set of nonlinear tensor elements that is consistent with our data. From Eqs. (9), (10), (11), and (12), we can relate the relative values of the nonlinear susceptibility tensor elements to the measured complex quantities η and κ via

$$\frac{\chi^{(2)}_{\parallel}}{\chi^{(2)}_{BULK}} = \frac{1}{2\kappa} \frac{\epsilon_1}{k_1} \frac{k_{1z}+k_{2z}}{\epsilon_2 k_{1z}+\epsilon_1 k_{2z}} \frac{k_x}{\sin\theta_T} \frac{t_S}{t_P} \tag{13}$$

and

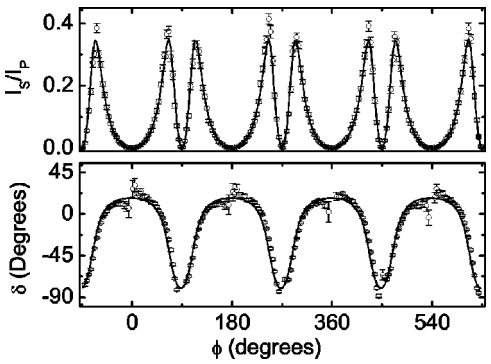

FIG. 6. Second-harmonic light generated from Sample 1 fitted to Eqs. (9) and (10). The input polarization was varied through a full rotation of the input half wave plate (see Fig. 2), resulting in four full rotations of the input polarization vector. The fitting results in $|\eta| = 2.89 \pm 0.02, \phi_\eta = (18.1 \pm 0.3)°, |\kappa| = 0.58 \pm 0.01$, and $\phi_\kappa = (-80.4 \pm 0.5)°$ with a $\chi^2 = 3.7$. The value of χ^2 differs from unity because of systematic errors near *s* and *p* input polarization, where *s*-polarized SHG decreases to zero, and $\delta^{(2\omega)}$ becomes very sensitive to systematic errors in calibration.

$$\frac{\chi^{(2)}_{\perp}}{\chi^{(2)}_{BULK}} = 2\frac{\chi^{(2)}_{\parallel}}{\chi^{(2)}_{BULK}} \left(\frac{t_S}{t_P} \frac{k_1}{k_x} \frac{\epsilon_2 k_{1z}+\epsilon_1 k_{2z}}{\epsilon_1 (k_{1z}+k_{2z})} \frac{\eta}{\sin\theta_T} - \frac{k_{2z}}{k_x} \frac{\cos\theta_T}{\sin\theta_T} \right) - \frac{\cos^2\theta_T}{\sin^2\theta_T} - 1. \tag{14}$$

Clearly, in addition to η and κ, we need the linear optical constants to allow analysis of $\chi^{(2)}$.

In order to determine the linear optical constants necessary for evaluation of Eqs. (13) and (14), we used a combination of spectroscopic variable angle ellipsometry[16] to determine optical properties and atomic force microscopy (AFM) to determine surface morphology. We used the ellipsometer to measure $\Psi^{(1)}$, which characterizes the relative linear reflectivity of the films through $\tan\Psi^{(1)} = |r_P|/|r_S|$, where r_P and r_S are the linear reflectivities of *p*- and *s*-polarized light and Δ, the relative phase of the reflected *p*- and *s*-polarized light. For each film, data were taken with incident light varying from 300 nm to 900 nm and at multiple angles of incidence. For each film, multiple AFM images were taken and the resulting root-mean-squared (rms) roughness calculations were averaged. The variation in the roughness measurements for a given film was typically 0.1–0.3-nm rms. A sample image is shown in Fig. 7. The roughness of each film is shown in Table I. The rms roughness of the silicon dioxide/silicon substrates was found to be 0.8 nm. The ellipsometer data were modeled in a way consistent with the AFM results and the known surface oxide of Al in order to obtain numerical values for the linear optical constants.

Again, ellipsometric data suffers from an inversion problem in that it is impossible to determine the exact surface morphology from ellipsometric data alone.[17] For our data, we investigated several models for the film surfaces, all of which generated excellent fits to the optical data. For each model, the structure of the surface is fixed and the linear optical constants of the Al (determined from a three Lorent-

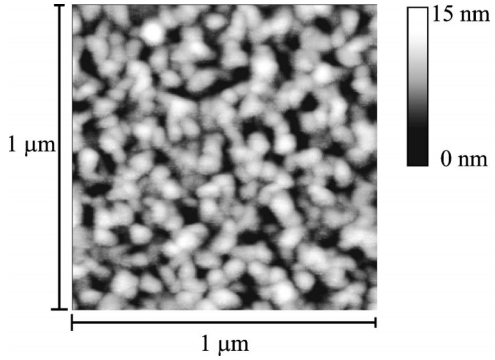

FIG. 7. One-μm^2 atomic force microscopy image of an Al film (Sample 3). The granular appearance of the image suggests many nanocrystalline orientations within the typical 10 μm focal spot of our Ti:sapphire laser. This film shows a root-mean-square roughness of 2.4 nm.

zian model for the dielectric function) are varied in order to produce the best match to the experimental data.

We considered three major models: (1) film surfaces modeled as a bare Al/air interface, (2) films with a top Al/Al_2O_3(20 Å)/air interface, and (3) films with a surface that included a roughness layer mixing Al, Al_2O_3, and air that was consistent with the AFM results. All three models produced statistically identical fits to the ellipsometric data. In Fig. 8, we show results for sample 3. The top two graphs show the fitting results for the third model (that includes a roughness layer consistent with the AFM results) along with the experimental data for $\Psi^{(1)}$ and Δ. Additionally, results

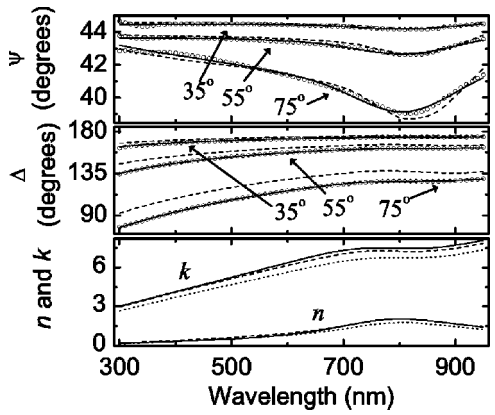

FIG. 8. Comparison of ellipsometer fitting for different models of the Al surface for sample 3. In the top two plots, solid lines show the fit result to a simple metal/air interface. The angle of incidence for each data set and fit is noted on the figure. Fitting results for other models of the Al surface are indistinguishable from the solid lines. For comparison, dashed lines in these two plots show results generated by using a simple air/Al interface with tabulated values for the Al optical constants from *Handbook of the Optical Constants of Solids* (Ref. 18). In the lower plot, the Al optical constants, *n* and *k*, are plotted for three successful models of the Al surface: solid lines result from a model that includes surface roughness and an oxide layer; dashed lines result from a model that assumes a 20-Å surface oxide; and dotted lines result from a simple metal/air interface.

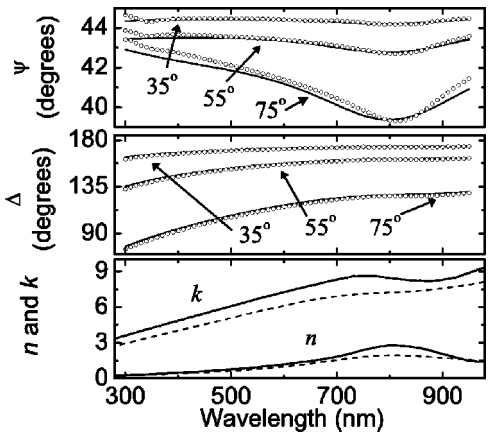

FIG. 9. Ellipsometric data (Ψ and Δ) from sample 3 and fit to a model for the film surface that includes a roughness layer consistent with AFM results and uses a three-Lorentzian model for the dielectric constant of Al are shown in the top two graphs. The lower graph shows the optical constants, *n* and *k*, that result from the fit (dashed lines) and, for comparison, the tabulated values for *n* and *k* for aluminum taken from *Handbook of Optical Constants of Solids* (Ref. 18) (solid lines).

are plotted from a model including a simple Al/air interface using tabulated values for Al optical constants.[18] In the lower graph, the real and imaginary parts of the index of refraction, *n* and *k*, for the Al film are shown for the three successful models mentioned above.

Because multiple models were successful in fitting the ellipsometric data, we have chosen to use a model believed to be the most consistent with AFM results. The data for all of the films were simultaneously fitted to a model that includes the silicon wafer, the silicon dioxide layer, a three-Lorentzian optical model for the Al dielectric constant, an Al_2O_3 layer, and a roughness layer. For the five films found to be optically thick, the aluminum layer was set to have a thickness that was consistent with the sputtering time and conditions. The roughness layers were set equal to the values measured with AFM. The fit was allowed to vary the optical constants of the aluminum, the thickness of the two optically thin films, and the relative content of the Al_2O_3/roughness layer. Fit results for sample 3 and a comparison of the fitted Al optical constants to the tabulated values for *n* and *k* are shown in Fig. 9. This model resulted in indices of refraction of $n=1.94$ and $k=7.24$ at $\lambda=810$ nm and $n=0.43$ and $k=4.08$ at $\lambda=405$ nm. The results of other models suggested that our determination of the linear optical properties were only good to $\pm 10\%$, with the major source of uncertainty being our ignorance of the precise surface conditions. The robust values of *n* and *k* that we find for the various models give us confidence in the further analysis of η and κ to yield the elements of $\chi^{(2)}$.

The details of the film surface are also relevant to the model used in SHG calculations. In Sec. II, we assumed that the surface was a simple metal/air interface. However, because our Al films were air exposed, a more accurate model would include details of the surface structure. We studied the effect a layer of Al_2O_3 would have on the second-harmonic reflection efficiency as follows: We compared the simple

TABLE II. Measured magnitudes and relative phases of the nonlinear susceptibility tensor elements for the films shown in Table I.

Sample	$\chi_{\perp}^{(2)}$ ($cm^2/statVolt \times 10^{-16}$)	$\phi_{\perp} - \phi_{BULK}$ (degrees)	$\chi_{\parallel}^{(2)}$ ($cm^2/statVolt \times 10^{-16}$)	$\phi_{\parallel} - \phi_{BULK}$ (degrees)	$\chi_{BULK}^{(2)}$ ($cm^2/statVolt \times 10^{-16}$)
1	2443 ± 485	10 ± 6	13.9 ± 2.7	85 ± 3	9.0 ± 1.8
2	2155 ± 424	3 ± 5	12.9 ± 2.5	64 ± 2	7.2 ± 1.4
3	2083 ± 334	-9 ± 5	11.5 ± 2.2	56 ± 3	7.2 ± 1.4
4	2400 ± 469	-1 ± 5	12.9 ± 2.4	65 ± 3	8.1 ± 1.6
5	2015 ± 477	-8 ± 5	13.4 ± 2.7	60 ± 3	7.6 ± 1.4
6	1527 ± 302	3 ± 5	11.4 ± 1.9	48 ± 4	7.6 ± 1.4
7	1810 ± 392	-1 ± 5	8.9 ± 1.6	53 ± 3	8.1 ± 1.6

model (described in Sec. II) that has an abrupt metal/air interface with one that includes the oxide layer.[10] This model assumed that all SHG occurred at the oxide/Al interface and was generated by an electric field that had been transmitted through the oxide. The reradiated second-harmonic electric field was calculated by satisfying the boundary conditions for the linear and second-harmonic fields at the air/oxide and oxide/Al interfaces. The ellipsometry measurements suggested that the oxide layers on our films were about 20 Å thick. Our model showed that the effect of a 20 Å layer of oxide resulted in changes in the values of the tensor elements that were much smaller than the statistical error in our data. For this reason, the effects of an oxide layer are neglected in the calculations of the reradiated second-harmonic electric field presented here.

We then used the optical constants at ω and 2ω with the fitted values for η and κ to deduce the relative magnitudes and phases of $\chi_{BULK}^{(2)}, \chi_{\perp}^{(2)}$, and $\chi_{\parallel}^{(2)}$. Because the statistical error in η and κ is much smaller than the uncertainty in the complex index of refraction arising from model-choice, the dominant source of uncertainty in the relative values of $\chi_{BULK}^{(2)}, \chi_{\perp}^{(2)}$, and $\chi_{\parallel}^{(2)}$ is the uncertainty in choice of optical model for the linear optical constants.

Finally, we convert the relative values of $\chi^{(2)}$ to absolute values by using the calibrated gain of our system. We calibrated the overall optical gain of the system using bulk SHG from a 4 mm *y*-cut quartz plate.[6] The crystal was rotated so that the *x* axis was positioned parallel to the polarization of the incident beam. As reported by Angerer *et al.*,[19] Maker fringes[20] are not observed because of the group velocity mismatch of the bound and free waves associated with the broad optical bandwidth of the incident Ti:sapphire pulses. A summary of the calculations necessary to determine the amplitude of the second-harmonic electric field generated from bulk SHG in quartz is shown in the Appendix.

The resulting absolute magnitudes and relative phases of the elements of $\chi^{(2)}$ are shown in Table II. The uncertainties reported for the amplitudes and relative phases of $\chi_{\perp}^{(2)}$ and $\chi_{\parallel}^{(2)}$ represent the propagated uncertainty of 10% in the optical constants of the Al films in the calculations of the relative amplitudes and phases of $\chi_{\parallel}^{(2)}$ and $\chi_{\perp}^{(2)}$ with respect to $\chi_{BULK}^{(2)}$. The uncertainties reported for the magnitude of $\chi_{BULK}^{(2)}$ represent the uncertainty in the optical constants and the uncertainty in the calibrated gain of our system, propagated through the calculation of the absolute values of the

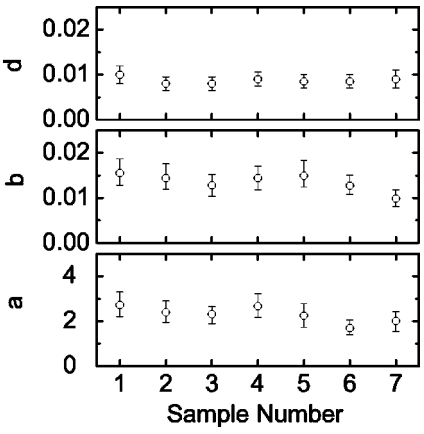

FIG. 10. Magnitudes of the dimensionless parameters *a*, *b*, and *d* that characterize the second-harmonic response. Error bars in the top plot show the error arising from uncertainty in the linear optical constants propagated through the determination in absolute intensity. In the two lower plots, the error bars show the error arising from the uncertainty in the linear optical constants propagated through the calculation of the relative magnitudes of the surface polarization parameters *a* and *b* to the bulk parameter *d*.

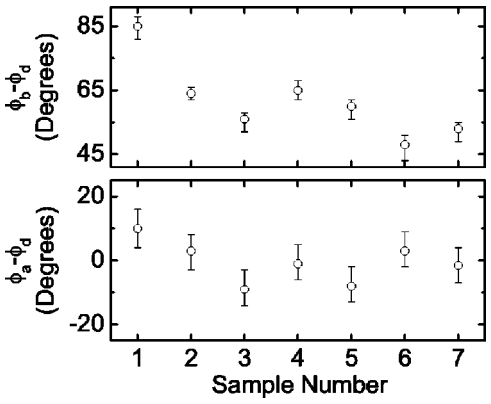

FIG. 11. Relative phases of *a* and *b* to *d*. Error bars show the error arising from the uncertainty in the linear optical constants propagated through the calculation of the relative phases of the surface polarization parameters *a* and *b* to the bulk parameter, *d*. The absolute phase is not determined.

tensor elements. This uncertainty is also present in the reported values for $\chi_{\parallel}^{(2)}$ and $\chi_{\perp}^{(2)}$. We also calculated the dimensionless parameters, a,b, and d, which are shown in Figs. 10 and 11 using Eq. (7), with $\epsilon(\omega)$ determined from $n(\omega)$ and $k(\omega)$ and m set to the free electron mass. As in Table II, the error bars in a and b reflect the propagated error in the optical constants in the calculation of the relative values and phases to d while the error bars in the plot of d reflect the error in the calculation in the overall gain of the system.

Multiple films were measured in order to determine if there was any correlation between the film surface morphology and the resulting nonlinear optical properties. The data shows that the results for all of the films are very similar. The only correlation between film properties and optical properties that we could determine is that Samples 6 and 7, which were optically thin, showed smaller amounts of SHG for p-input polarization, resulting in smaller values of $\chi_{\perp}^{(2)}$ (see Table II). It seems unlikely that interference from the backside of the Al film could be responsible for this suppression of $\chi_{\perp}^{(2)}$, since the magnitude of the squared transmitted electric field is approximately 30 times smaller due to transmission through the Al film. These films are also the two smoothest films, suggesting that the magnitude of $\chi_{\perp}^{(2)}$ is, perhaps, smaller for smooth films, in qualitative agreement with previous measurements.[21]

V. DISCUSSION

Comparison of our results for the measured surface current perpendicular to the surface of Al shows relatively good agreement with previous theoretical and experimental work. We find an average value of $|a|=2.30\pm0.72$, which is smaller than the predicted value of LS for the bare Al/vacuum interface, but consistent with the observed suppression of Al SHG due to oxide overlayers in the p-input, p-output geometry.[8]

Despite this agreement on the value of a between our measurements and past work, we find strong disagreement between our measured values of b and d and theoretical expectations. We find average values of $|b|=0.014\pm0.004$,$|d|=0.009\pm0.002$, and $\phi_b-\phi_d=63\pm12°$. This is in contrast to the expectations for b and d shared by hydrodynamic, Boltzmann, and density functional treatments. These models predict that $b=-1$ for smooth surfaces and $b<1$ for rough surfaces. However, decreases in b due to surface roughness are expected to be small (less than a factor of 2) and do not easily account for our measured value that is 100 times smaller than predicted. For d, these models are fairly simplistic and agree on the value $d=1$. Additionally, d is expected to be robust to changes in surface conditions, making our measured value even more difficult to explain. These discrepancies lead us to carefully consider both the small observed values of b and d and their relative phase.

A simple explanation for the small measured size of b and d is that our calibration of gain is incorrect. As a cross check of the gain calibration, we have compared the calculated gain using quartz crystals with an estimation of the gain using the known input pulse shape, input power, laser repetition rate, PMT sensitivity, and amplifier gains of the system. The cross check demonstrates that our calibrated gain is reasonable. Additionally, our overall agreement on the size of a with other experimental work suggests that our calibration is correct. If our calibration did indeed underestimate the gain of the system in order to explain the deviation from expected results (this would require an error of 10^4 in intensity), it would imply that our measured value of a was an order of magnitude larger than that found for bare Al/vacuum interfaces, contradicting both theoretical and past experimental work. Lastly, we note that while an error in gain might explain the small observed magnitudes of b and d, it cannot explain the relative phase of b and d, which, at 63°, deviates significantly from the theoretical expectation of 180°.

For the reasons above, we believe that our gain is correct and, therefore, consider possible physical explanations for the small observed b and d. One could imagine that the value of $|b|$ is suppressed due to surface oxidation, much as is observed for $|a|$. This hypothesis contradicts theoretical models that expect $|b|$ to be insensitive to the details of the electronic surface structure, and would furthermore not explain the small value of $|d|$, which arises from bulk contributions and should be largely independent of the details of the surface. Regarding the small d values, one could consider the possibility that the surface tensor elements $\chi_{ZXX}^{(2)}$ and $\chi_{ZYY}^{(2)}$ are nonzero. Theoretical models predict these elements to be zero due to continuity of the electric field component tangential to the surface. If these elements were nonzero, they could in principle cause destructive interference with the bulk SHG and suppress the effective value of $|d|$. However, this hypothesis does not help explain the suppression of $|b|$, which arises entirely from a single surface contribution, $\chi_{YZY}^{(2)}=\chi_{YYZ}^{(2)}$.

As mentioned above, previous experiments have also demonstrated disagreement with theoretical predictions for b and d. In particular, Janz *et al.*[6] " . . . found that there was no measurable component of s-polarized SH light at any wavelength or angle of incidence available to us." Thus, Janz *et al.* found $|b|\approx0$ while $|a|\approx30$ for their bare UHV Al surfaces. The measurable effect of surface charge on bulk SHG from Ag, as observed by Simpson and Furtak,[11] also contradicts a jellium-type model for SHG. However, their suggestion that this effect is due to an alteration of the tail of the bulk free-electron density seems likely to only lead to a small suppression of $d(\omega)$ rather than the large effect that we have observed.

Collectively, our experimental results as well as results from UHV Al surfaces and charged electrolyte/Ag interfaces show significant variation in the parameters b and d, but consistent results for a. This observation is in contrast to theoretical predictions suggesting that a is very sensitive to the details of the surface, but that b and d are relatively robust to the surface conditions. While many of these approaches are essentially free-electron-gas calculations, and therefore ignore interband transitions and the associated physics, most allow for at least approximate modification to obtain a more realistic response. For example, the classical models can include finite-frequency Lorentzian oscillators

and generate good approximate linear optical susceptibilities. Similar improvements for the associated nonlinear calculations still lead to Eqs. (7), but with improved values of $\epsilon(\omega)-1$ as compared to experiment, but no change in the prediction that $|b|$ and $|d|$ are unity.[22] At present, we believe that our results highlight the fact that essentially all of the simple models, whether hydrodynamic, Boltzmann, or density functional jellium (that provide the most accurate predictions for a), lack some crucial physics necessary for a deeper understanding of nonlinear optical processes.

VI. CONCLUSION

We have measured the complete amplitude and relative phases of the nonlinear susceptibility tensor elements responsible for second-harmonic generation at the surface of a variety of air-exposed Al films. The measurements show that the seven-element surface nonlinear susceptibility tensor for an isotropic system adequately explains the observed surface SHG for these isotropic films. Additionally, the data and analysis show that the complex parameters η and κ can conveniently characterize SHG from an isotropic surface for any particular angle of incidence and fundamental frequency.

We have also used the measured values of η and κ using a specific model for our surface in order to determine the nonlinear currents in the surface and bulk of the Al films. The analysis shows that the surface currents perpendicular to the surface of the films are consistent with previous calculations and experiments. However, the analysis also shows that the currents parallel to the surface and in the bulk of the aluminum are dramatically smaller than is predicted by theoretical calculations. This discrepancy indicates a need for development of a more accurate understanding of the effective bulk susceptibility and of the susceptibility due to surface currents parallel to the surfaces of such films.

ACKNOWLEDGMENTS

We gratefully acknowledge the support of the National Storage Industry Consortium via the Extremely High Density Recording program, the Colorado Center for Information Storage, the National Science Foundation through the Optical Science and Engineering Program at the University of Colorado at Boulder, and partial support from the Army Research Office through the DURINT Program Grant No. DAAD-19-01-1-0521. We also acknowledge assistance from Feng Pan and Sugantha Mani for x-ray diffraction work.

APPENDIX: QUARTZ CALIBRATION

In order to accurately describe the second-harmonic electric field generated from a quartz crystal by femtosecond-duration electric fields, it is necessary to take into account the full spectrum of the incident electric field. The broad spectrum of Ti:sapphire sources causes significant bandwidth in the second-harmonic light in the bulk of the crystal and the associated loss of Maker fringes for sample thicknesses greater than 0.5 mm. We present the equations that we have used to calibrate our SHG experiment so that this work can be easily compared to future experiments. In this analysis, we follow the procedure shown by Angerer *et al.*[19]

For a Gaussian electric field pulse propagating through the vacuum in the $\hat{z}$ direction, polarized in the $\hat{x}$ direction, and with a central frequency of ω_0, we may write our electric field frequency distribution as

$$\vec{E}(\omega)=\frac{E_0}{\Delta\omega}\hat{x}e^{-(\omega-\omega_0)^2/\Delta\omega^2}e^{\imath(\omega_0/c)z}. \tag{A1}$$

Here, c is the speed of light in the vacuum and $\Delta\omega=1/\Delta t$ is the inverse of the electric field pulse duration, and E_0 is the peak magnitude of the electric field. If this pulse is normally incident on a section of y-cut quartz with its $\hat{x}$ axis aligned with the $\hat{x}$ direction, then it will induce a nonlinear polarization distribution in the bulk of the quartz according to[23,24]

$$\begin{aligned}\vec{P}(\omega)&=\int\int d\omega_1 d\omega_2 \epsilon_0 d_{11}\vec{E}(\omega_1)\vec{E}(\omega_2)\delta(\omega-\omega_1-\omega_2)\\&=\frac{\epsilon_0}{\Delta\omega}\hat{x}\sqrt{\frac{\pi}{2}}d_{11}t^2E_0^2e^{-(\omega-2\omega_0)/2\Delta\omega^2}e^{\imath 2k(\omega)z},\end{aligned} \tag{A2}$$

where, d_{11} is the nonlinear susceptibility of quartz (0.3 pm/V),[25] t is the transmission Fresnel coefficient at the fundamental frequency ω_0, and $k(\omega)=n(\omega)\omega/c$ is the wave vector inside the quartz. This nonlinear polarization acts as a source term in Maxwell's equations that results in a particular solution (often called the ''bound'' wave) to the wave equation,

$$\vec{E}_B(\omega)=\left[\frac{\mu_0 c^2\vec{P}(\omega)}{n^2(\omega)-n^2(2\omega)}\right]. \tag{A3}$$

Along with the bound wave, there are also four ''free'' waves (the reflected second-harmonic beam, the transmitted second-harmonic beam, and forward and backward multiply reflected waves in the quartz plate) that satisfy the homogeneous wave equation. The amplitudes of these waves can be determined by satisfying the boundary conditions at the front and back surfaces of the crystal.[26] Including all four waves in the calculation results in a fine oscillatory dependence on sample thickness that is superimposed on the traditional Maker fringes.[20] For the purposes of this calculation, this fine structure can be neglected and we can write the transmitted nonlinear wave as

$$\vec{E}_T(\omega)=\vec{E}_B(\omega)\frac{4k_F}{k_0+k_F}\sin(\Psi), \tag{A4}$$

where $\Psi=(k_B-k_F)L, k_B=2k(\omega)$ is the bound wave vector, $k_F=k(2\omega)$ is the free wave vector, and L is the thickness of the quartz plate. For a monochromatic wave, the $\sin(\Psi)$ factor results in traditional Maker fringes. The last step in the analysis is to expand the wave vectors in the phase of the

electric field to first order in $\omega-\omega_0$ and to Fourier transform back into the time domain:

$$\vec{E}_T(t)=\left[\frac{2\sqrt{2\pi}d_{11}t^2E_0^2\Delta t}{n^2(\omega)-n^2(2\omega)}\right]\frac{k_F}{k_0+k_F}e^{\imath 2\omega t}\times[e^{\imath\Psi}e^{-(1/2)[\Delta\omega(DL-t)]^2}-e^{-\imath\Psi}e^{-(1/2)[\Delta\omega(DL+t)]^2}], \tag{A5}$$

where $D=(\partial k/\partial\omega)|_{\omega=\omega_0}-(\partial k/\partial\omega)|_{\omega=2\omega_0}$. The transmitted second-harmonic electric field separates into two Gaussian pulses that only interfere to produce Maker fringes when the product of the material dispersion and thickness are small compared with the duration of the pulse. In our experiment, the two pulses do not overlap appreciably and the measured second-harmonic intensity is not sensitive to the exact quartz thickness.

*Electronic address: Charles.Teplin@Colorado.EDU

[1] See, for example, Y.R. Shen, Annu. Rev. Phys. Chem. **40**, 327 (1989).
[2] N. Bloembergen, R.K. Chang, S.S. Jha, and C.H. Lee, Phys. Rev. B **174**, 813 (1968).
[3] J. Rudnick and E.A. Stern, Phys. Rev. B **4**, 4274 (1971).
[4] A. Liebsch and W.L. Schaich, Phys. Rev. B **40**, 5401 (1989).
[5] R. Murphy, M. Yeganeh, K.J. Song, and E.W. Plummer, Phys. Rev. Lett. **63**, 318 (1989).
[6] S. Janz, K. Pedersen, and H.M. van Driel, Phys. Rev. B **44**, 3943 (1991).
[7] S. Janz and H.M. van Driel, Int. J. Nonlinear Opt. Phys. **2**, 1 (1993).
[8] S. Janz, K. Pedersen, H.M. van Driel, and R.S. Tismit, J. Vac. Sci. Technol. A **9**, 1506 (1991).
[9] K. Pedersen and O. Keller, J. Opt. Soc. Am. B **6**, 2412 (1989).
[10] J.C. Quail and H.J. Simon, Phys. Rev. B **31**, 4900 (1985).
[11] L.J. Simpson and T.E. Furtak, J. Electroanal. Chem. **500**, 163 (2000).
[12] P. Guyot-Sionnest, W. Chen, and Y.R. Shen, Phys. Rev. B **33**, 8254 (1986).
[13] Kurt. J. Lesker Company.
[14] Pacific Silicon Sensor Inc. model PSS-DL100-7PCBA.
[15] As the input polarization moves through pure *s*- or *p*-incident polarization, the fitted second-harmonic polarization state results in values of $S2$ that approach zero and change sign. The exact location of this transition in $S2$ is very sensitive to the calibration of the polarimeter. Since $\tan\delta=(S3/S2)$, the value of δ becomes very sensitive to the value of $S2$ at these points. Since statistical error at these points does not account for the dominant deviation arising from small errors in calibration, we chose not to fit δ at these points in order to obtain values of χ^2 that are more representative of the statistical error in the data.
[16] J.A. Woollam Co., Inc. VASE system.
[17] R.M.A. Azzam and N.M. Bashara, *Ellipsometry and Polarized Light* (Elsevier North-Holland, Amsterdam, 1977).
[18] Edward D. Palik, *Handbook of Optical Constants of Solids* (Academic Press, New York, 1985).
[19] W.E. Angerer, N. Yang, A.G. Yodh, M.A. Khan, and C.J. Sun, Phys. Rev. B **59**, 2932 (1999).
[20] J. Jerphagnon and S.K. Kurtz, J. Appl. Phys. **41**, 1667 (1970).
[21] O.A. Aktsipetrov, A.A. Nikulin, V.I. Panov, S.I. Vasil'ev, and A.V. Petukhov, Solid State Commun. **76**, 55 (1990).
[22] B.S. Mendoza and W.L. Mochan, Phys. Rev. B **53**, 4999 (1996).
[23] Since this section is designed to determine the size of a second-harmonic field from a quartz crystal that is used as an experimental calibration, we have chosen to do this calculation in mks units.
[24] A.C. Newell and J.V. Moloney, *Nonlinear Optics* (Addison-Wesley, Redwood City, California, 1992).
[25] V.G. Dmitriev, G.G. Gurzadyan, and D.N. Nikogosyan, *Handbook of Nonlinear Optical Crystals*, 2nd ed. (Springer-Verlag, Berlin, 1997).
[26] W.N. Herman and L.M. Hayden, J. Opt. Soc. Am. B **12**, 416 (1995).